







Orthogonally polarized semi-polar (20 $\bar{2}1$) InGaN/GaN-based MCLED array

QINGLIN JIA,¹ JINGFENG DUAN,¹ WEI OU,² MINGSHUANG MA,¹ 
LEIYING YING,¹ NING WANG,³ YIKUN BU,³   YANG MEI,^{1,*}  AND
BAOPING ZHANG^{2,4}

¹Laboratory of Micro/Nano-Optoelectronics, School of Electronic Science and Technology, Xiamen University, Xiamen 361005, China

²Institute of Nanoscience & Applications, Southern University of Science and Technology, Shenzhen 518055, China

³Fujian Key Laboratory of Ultrafast Laser Technology and Applications, Xiamen University, Xiamen, Fujian 361005, China

⁴bzhang@xmu.edu.cn

*meiyang@xmu.edu.cn

Abstract: Orthogonally polarized light technology holds significant promise for applications in visible light communication, 3D displays, and medical imaging. This study introduces a novel semi-polar (20 $\bar{2}1$) InGaN/GaN-based microcavity light-emitting diode (MCLED) capable of simultaneously generating orthogonally polarized light parallel and perpendicular to the [10 $\bar{1}\bar{4}$] axis. An optical resonant cavity was formed by employing SiO₂/TiO₂ distributed Bragg reflectors (DBR) and Ag as reflectors, enhancing thermal dissipation and achieving a high polarization ratio (~ 0.89). A parallel MCLED array was fabricated, significantly improving output power while maintaining orthogonal polarization. This work advances orthogonally polarized light technology, offering new possibilities for practical applications.

© 2025 Optica Publishing Group under the terms of the [Optica Open Access Publishing Agreement](#)

1. Introduction

Polarized light sources hold great importance in both fundamental research and practical applications. It possesses a specific vibration direction, which can be utilized to reduce or eliminate glares and scattered light caused by light reflection. For instance, some automobile headlights employ polarizing filters to mitigate the glare to oncoming drivers [1–3]. Polarized light also plays a crucial role in the biomedical applications, such as employing polarized light microscopy to observe internal information of biological tissues and using infrared polarized light to treat migraines [4,5]. In display technologies, the application of polarized light can enhance image contrast and clarity, particularly under intense lighting or reflective environments. And the technology has been widely implemented in liquid crystal displays and 3D imaging fields [6,7]. For light communication, polarized multiplexing technology can significantly boost transmission efficiency, as it permits the simultaneous transmission of multiple data streams with different polarization states within a single optical fiber [8,9]. However, traditional polarized light technology still faces limitations in certain application scenarios, especially where higher demands for imaging contrast and clarity are required, as factors such as surface reflection and background noise may preclude conventional polarized light imaging from providing adequate detail and clarity [10,11]. To overcome these limitations, researchers have developed orthogonal polarized light technology [12], where two polarized light beams with perpendicular polarization directions effectively suppress interference caused by surface reflection, thereby enhancing imaging contrast and clarity [13,14]. The advantage of orthogonal polarized light technology lies in its ability to provide more refined structural imaging, which is particularly important in medical imaging, material inspection, and other fields [15–17].

The acquisition of orthogonally polarized light is a complex process that requires the addition of a quarter-wave plate to a polarizer. When the fast axis of the quarter-wave plate is at a 45° angle to the polarization direction of the linearly polarized light, the light passing through the quarter-wave plate will transform into circularly or elliptically polarized light. After traversing another polarizing filter, two orthogonal linearly polarized light components can be obtained. Similarly, a half-wave plate can also be used to convert polarized light into orthogonal polarized light [18]. Although the methods of obtaining orthogonal polarized light using polarizing filters, quarter-wave plates, or half-wave plates are quite effective both theoretically and practically, the process necessitates the assembly of multiple optical components and precise adjustment of the optical path, which undoubtedly increases the loss in the optical path. Moreover, the complex assembly of the system not only entails higher costs but may also result in system instability. Therefore, optimizing the acquisition method of orthogonal polarized light is of paramount importance. To this end, it is desirable to simultaneously obtain a set of orthogonally vertical polarized lights within the same light-emitting device. Gallium nitride (GaN), as a semiconductor material with exceptional optoelectronic properties, can achieve luminescence across a spectrum ranging from deep ultraviolet to near-infrared by adjusting the concentrations of indium (In) and aluminum (Al) in the active region [19–22]. In wurtzite GaN based materials, the inherent hexagonal symmetry induces a crystal field that results in the splitting of the valence band into two distinct subbands. Upon the inclusion of spin-orbit coupling effects, the valence band undergoes further splitting, giving rise to the heavy-hole (HH) band, light-hole (LH) band, and crystal-field split hole (CH) band [23]. Nevertheless, since GaN materials are typically epitaxially grown on sapphire substrates along the [0001] axis, which exhibits high symmetry and induces relatively small separation between the HH and LH bands. Consequently, the intensities of spontaneous emission originating from the recombination of carriers from the conduction band to the HH band and to the LH band are nearly identical, generally exhibiting no obvious polarization [24]. Research has demonstrated that semi-polar InGaN/GaN-based LEDs epitaxially grown on sapphire substrates along the $[20\bar{2}1]$ axis exhibit polarized luminescence characteristics. This phenomenon is primarily attributed to the unbalanced biaxial stress in semi-polar InGaN/GaN quantum wells (QWs) structures, which enhances the separation between HH and LH bands, resulting in spontaneous emission of light with two distinct wavelengths and different intensities from these bands [25,26]. For semi-polar $(20\bar{2}1)$ InGaN/GaN-based LEDs, the direction of spontaneous emission from the LH band is parallel to the $[10\bar{1}\bar{4}]$ axis, while that from the HH band is perpendicular to the $[10\bar{1}\bar{4}]$ axis, combining to form a set of orthogonal polarized lights [27]. However, the ratio of polarization in traditional semi-polar InGaN/GaN-based LEDs is not high, typically to be 20-50% [28]. In systems employing polarization multiplexing for visible light communication, this can lead to crosstalk between signals, thereby increasing the bit error rate [29].

In our previous work, a resonant cavity with dual dielectric DBR ($\text{SiO}_2/\text{TiO}_2$) structure was integrated with semi-polar LEDs to enhance the ratio of polarization [30]. Due to the birefringent properties of semi-polar GaN, light waves with different polarization directions propagate through the GaN material are featured with distinct refractive indices [31], leading to different resonant wavelengths. Therefore, the emission with orthogonally polarization can be spectrally separated by introducing a resonant cavity with narrow mode linewidth. The dual dielectric DBR cavity structure can offer advantages such as high reflectivity, extremely narrow linewidths, and a high ratio of polarization. However, this structure still presents certain limitations, such as poor heat dissipation, low output power, and complex device fabrication processes [32–34].

In this study, orthogonally polarized semi-polar $(20\bar{2}1)$ InGaN/GaN-based MCLEDs was fabricated by employing $\text{SiO}_2/\text{TiO}_2$ DBR and Ag mirror as the top and bottom mirrors of the cavity. A high-ratio-of-polarization of 89% orthogonal polarized light source was successfully developed. The fabrication process is much simplified when compared with microcavity with dual

dielectric DBR structure, and heat dissipation can be effectively improved by the metal bottom mirror and copper substrate. The MCLED array was also fabricated to obtain higher output power. This work provides a novel approach for selecting polarized light sources in applications such as GaN-based high-speed visible light communication, 3D displays, and medical imaging.

2. Results and discussions

2.1. Device fabrication

The semi-polar (20 $\bar{2}$ 1) GaN based epilayers used in this study was grown on a patterned sapphire substrate (PSS) with (22 $\bar{4}$ 3) orientation using a metal-organic chemical vapor deposition (MOCVD) system [30]. The active region of the green epi-wafer contains a single InGaN QW with indium content of 0.25, and the detailed structure of the epi-wafer is illustrated in Fig. 1(a). Single QW structure was used in this study because we found that the brightness of epitaxial wafers was decreased when we grew InGaN multi-QWs on semi-polar GaN. The material growth is still needs to be improved in our future work. Figure 1(b) shows the structure of the single MCLED in this study. To fabricate the device, a 60 nm-thick indium tin oxide (ITO) film was first deposited on the p-type GaN layer using magnetron sputtering to facilitate lateral current spreading. Subsequently, a Cr/Ag (1 nm/150 nm) was sputtered onto the ITO film as the bottom mirror of the MCLED. To enhance the thermal dissipation of the MCLED, a 200 μ m-thick Cu layer was electroplated on the p-type GaN side of the structure, which also enable the following substrate transfer process. The PSS was then removed using laser lift-off (LLO) technology, exposing the u-GaN layer. The epitaxial layer thickness was thinned through chemical mechanical polishing (CMP), and the cavity length of the MCLED was controlled to approximately 2 μ m. A circular device mesa with a diameter of 70 μ m was formed by inductively coupled plasma (ICP) etching, and a SiO₂ layer was sputtered on the sidewalls for passivation. Finally, Cr/Au electrodes and two pairs of SiO₂/TiO₂ layers were sputtered as the top distributed Bragg reflector (DBR), forming a resonant cavity structure in conjunction with the Ag mirror. In addition to this, the grid array electrodes are designed in this work to ensure that the current can be injected uniformly into the MCLED arrays. This comprehensive fabrication process ensures the realization of a high-performance MCLED with optimized optical and thermal properties.

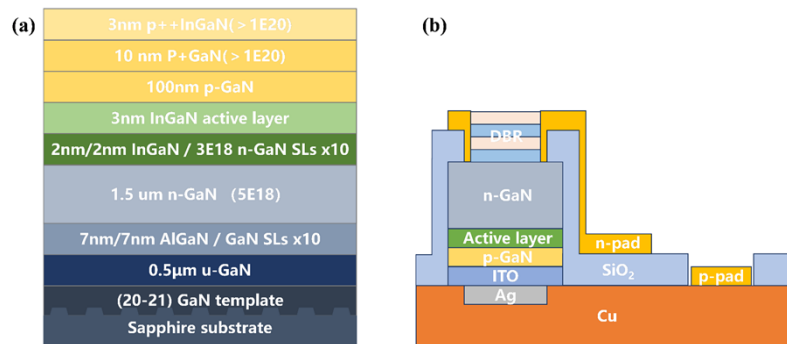


Fig. 1. Schematic diagrams of the semi-polar (20 $\bar{2}$ 1) plane InGaN/GaN epitaxial structure and the MCLED structure. (a) Illustration of the epitaxial structure. (b) Illustration of the MCLED structure.

Due to the poor adhesion of Ag when directly deposited on the surface of ITO, a 1 nm thick Cr layer was used as the adhesion layer between Ag and ITO in this study, given that Cr also exhibits high reflectivity in the green band. Figure 2(a) illustrates the relationship between the thickness of Ag layer and reflectivity. As the thickness of the Ag layer increases, reflectivity gradually increases and reaches saturation within the thickness range of 140 nm to 150 nm, where the

change in reflectivity is minimal. In the wavelength range of 500 nm to 570 nm, the reflectivity of Cr/Ag remains between 90% and 92%, whereas pure Ag can achieve high reflectivity of ~98%. Figure 2(b) depicts the trend of surface roughness of the Cr/Ag layer with increasing thickness, while Fig. 2(c) presents the corresponding atomic force microscopy (AFM) images of the Cr/Ag layers with different thicknesses. The root mean square (RMS) roughness of the Cr/Ag layer slightly increases with thickness. Although a larger surface roughness will degrade the reflectivity, the enhancement of reflectivity by the increase of Ag thickness is more pronounced here. Further increasing the thickness of Ag layer leads to a saturation of the reflectivity.

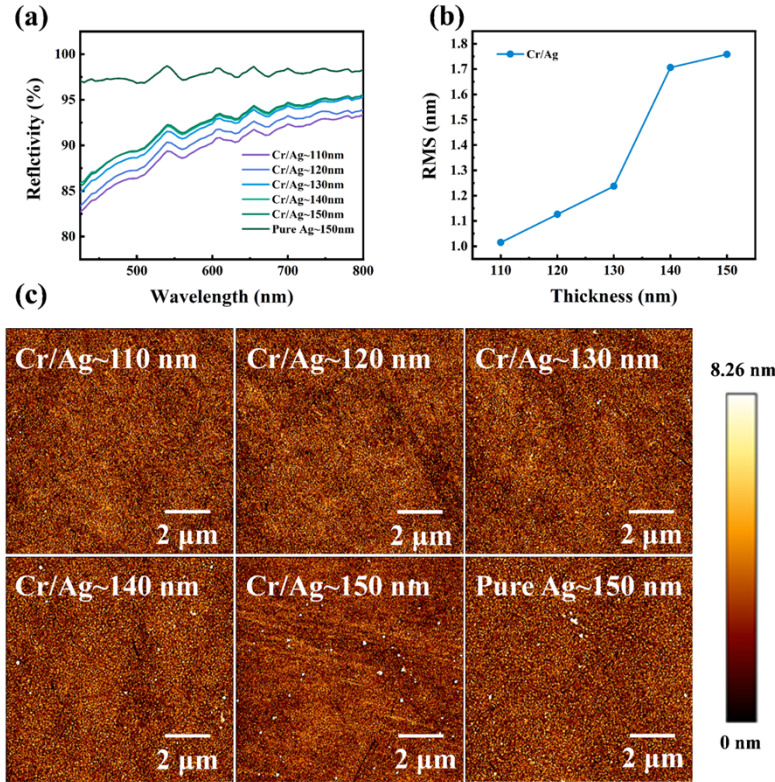


Fig. 2. (a) Reflectivity as a function of varying Cr/Ag thicknesses. (b) RMS roughness plotted against thickness. (c) AFM images at different thicknesses.

2.2. Orthogonal polarization emission characteristics of a single MCLED

Figure 3(a) presents the electroluminescence (EL) spectra of a semi-polar MCLED under different current. The emission spectra show several clear cavity modes at ~503, 528, 555, and 586 nm. However, very different with conventional c-plane RCLEDs [34], all cavity modes are splitted and comprises a main peak and a sub-peak. The mode splitting here are originated from the spontaneous emissions from the LH and HH band with orthogonal polarization, which will be discussed in detail later. As the injection current increases from 1 mA to 20 mA, each set of emission modes exhibit stable central wavelengths with negligible blue shift, and this is a unique superiority of MCLED when compared with normal LEDs without a cavity. For normal green Micro-LEDs, the emission wavelength usually shows a blueshift by 15-30 nm when the current density is increased to 1 kA/cm² due to the energy band filling effect [35–37]. In contrast, for MCLEDs, there is almost no blueshift as the injection current density increases. This property is

attributed to the wavelength selectivity of the microcavity. In MCLEDs, light is resonated inside the cavity, and the resonance condition is defined by $2nL = m\lambda$, where m is the resonance order, n is the refractive index, L is the cavity length. For the wavelengths matching with the resonate condition, the light will form standing waves inside the cavity, which is defined as the cavity modes, and the emission will be enhanced by interference. On the other hand, the emission at other wavelengths will be suppressed. This is why the emission spectra of the MCLED in this study show several narrow resonate peaks instead of the broad continuous spectrum of the normal LED. Therefore, the emission of the MCLED is determined by the resonate condition, which has no dependency on the injected current, and the emission wavelength is more stable than the normal LEDs without a cavity. Similar phenomenon has also been reported in other literatures [34]. Figure 3(b) illustrates the I-V curve under logarithmic coordinates for the current and the luminescence image at an injection current of 5 mA. At a current density of 20 mA/cm², the device exhibits a forward voltage (V_f) of 2.65 V. The reverse leakage current (I_r) measured at a voltage of -5 V was determined to be -9.97×10^{-7} A.

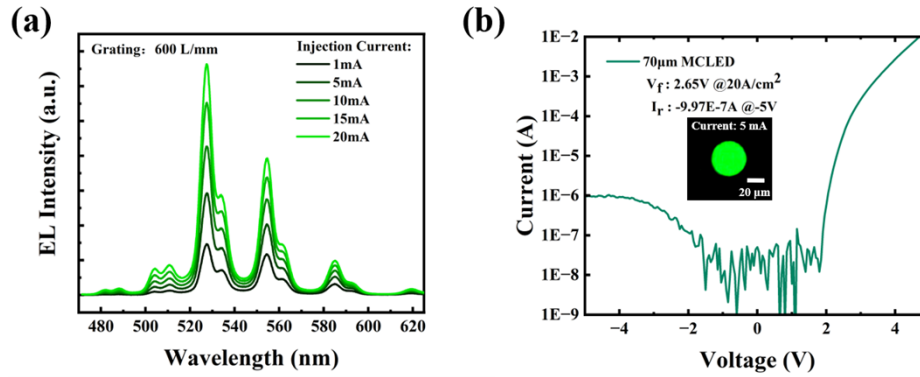


Fig. 3. (a) EL intensity of the MCLED. (b) I-V curve under logarithmic coordinates for the current.

The orthogonal polarization characteristics of the MCLED was measured by inserting a polarizer before the slit of the spectrometer and collecting EL spectra at varying polarization angles. Figure 4(a) illustrates the normalized EL spectra under several typical polarization angle between 0 and 180°. It can be clearly observed that the emission spectra are switched between two sets of optical modes with different polarization direction. When the polarizer angle is 0°(// $[10\bar{1}4]$), the spectrum consists a series of optical modes with single peak structure (Mode group I). While rotating the polarizer, another series of optical modes appears at shorter wavelength (Mode group II), and the intensity is gradually increased. Meanwhile, the intensity of Mode group I is suppressed, and the emission spectra are totally switched from Mode group I to Mode group II when the polarizer angle is 90°($\perp [10\bar{1}4]$). While increasing polarization angle between 90° and 180°, Mode group I appears again and gradually takes dominant. Figure 4(b) shows a contour map illustrating the relationship between wavelength, polarization angle, and luminescence intensity as the polarizer rotates from 0° to 180°. This figure distinctly reveals that Mode group I and II are orthogonally polarized. Note that the maximum intensity of Mode group I is smaller than that of Mode group II, this is because that the two groups of modes originates from the radiative recombination of electrons with holes in the LH and HH bands, respectively, and will be discussed in detail later.

The ratio of polarization (P) of Mode group I and II can be calculated using the following formula Eq. (1):

$$P = \frac{I_{max} - I_{min}}{I_{max} + I_{min}} \quad (1)$$

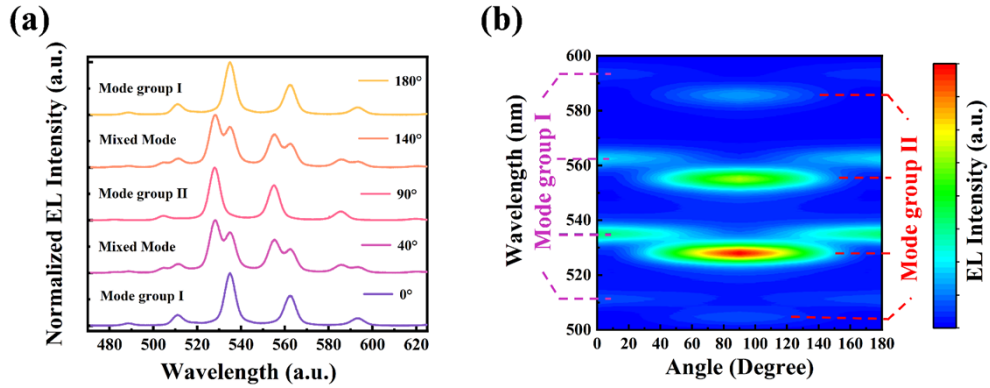


Fig. 4. (a) Normalized EL intensity plot corresponding to polarizer rotation from 0° to 180°. (b) EL intensity map of the MCLED.

where I_{\max} represents the maximum light intensity and I_{\min} represents the minimum light intensity under different polarization angle, respectively. The normalized intensity of Mode group I and II under different polarization angle are plotted under polar coordinates, as shown in Fig. 5. Based on formula 1, Mode group I and II both show high polarization ratio of 0.85 and 0.89. This result provides significant insights into the orthogonal polarization characteristics of semi-polar GaN based MCLEDs.

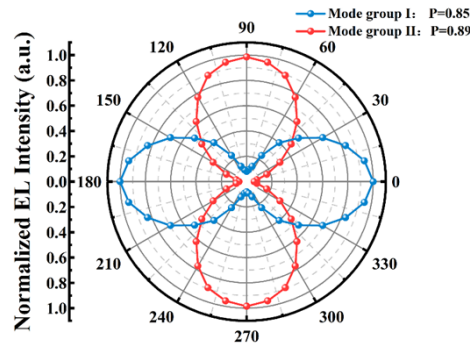


Fig. 5. Polar plot of the normalized EL intensity in polar coordinates.

In the crystalline structure of GaN materials, the inherent hexagonal symmetry, in conjunction with the spin-orbit coupling effect, induces a splitting of the valence band into distinct subbands, namely the HH band, LH band, and CH band. The biaxial compressive strain present in GaN/InGaN QWs further exacerbates the splitting of the valence band energy levels. Compared to c-plane grown InGaN/GaN crystals, the biaxial compressive stress in nonpolar and semipolar QWs is unbalanced, resulting in a greater separation between the HH and LH bands [24]. This allows electrons to recombine with holes in both the HH and LH bands to emit light. Additionally, since the electric dipole moments of the LH and HH bands are perpendicular to each other, the emitted light from these two bands has orthogonal polarization directions [23,38,39]. Figure 6(a) illustrates the relationship between the (20 $\bar{2}$ 1) plane and each crystal direction in the GaN hexagonal crystal system, where the c^* axis is the projection of the c axis on the (20 $\bar{2}$ 1) plane. Figure 6(b) shows a schematic diagram of a semipolar GaN crystal radiating orthogonally polarized light, where the yellow box corresponds to the (20 $\bar{2}$ 1) plane. where the direction of

polarization of the compound luminescence radiated by the heavy hole band is perpendicular to the c^* axis and the direction of polarization of the compound luminescence radiated by the light hole band is parallel to the c^* axis. Furthermore, the reduced symmetry of the semi-polar GaN crystal structure leads to anisotropic optical properties, which is characteristic of birefringent crystals [31]. Specifically, two orthogonal polarization components have distinct refractive indices. Therefore, when semi-polar InGaN was assembled within a cavity, the spontaneous emission from LH and HH with orthogonal polarization have different effective cavity lengths due to the distinct refractive indices, finally inducing different resonate wavelengths. This can well explain the origin of the mode splitting and orthogonal polarization of the Mode I and II from a single MCLED in this study.

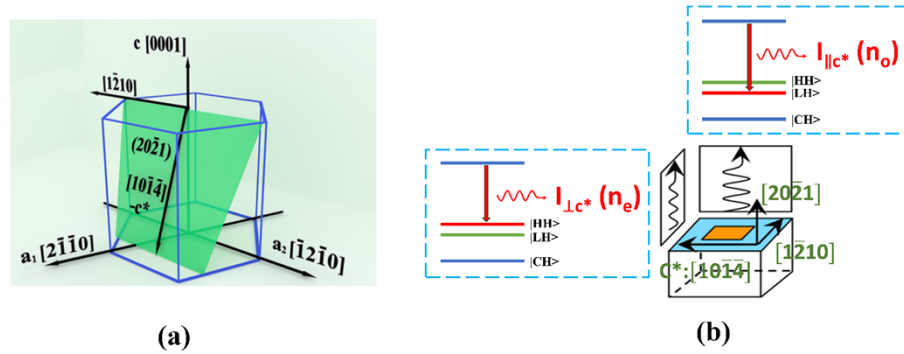


Fig. 6. (a) The relationship between the $(20\bar{2}1)$ plane and each crystal direction in the GaN hexagonal crystal system. (b) Schematic diagram of a semipolar GaN crystal radiating orthogonally polarized light.

The difference between the luminous wavelengths of LH band and HH band can be quantitatively analyzed by the resonance condition $2nL = m\lambda$. The product of physical cavity length L and refractive index n is the corresponding effective cavity length (L_{eff}). Table 1 shows the refractive index values of LH band and HH band luminescence in GaN crystals near the luminescence band of 500 nm [30,40].

Table 1. The values of refractive index and effective cavity length.

n	GaN	Physical cavity length(μm)	Effective cavity length(μm)
n_o	2.408	2.222	5.351
n_e	2.376	2.222	5.280

The calculated and experimental wavelengths of the cavity modes generated by the emission from LH and HH band are shown in Tables 2 and 3, respectively:

Table 2. Calculated and actual wavelengths of LH band luminescence.

m	$\lambda_{cal}(\text{nm})$	$\lambda_{exp}(\text{nm})$
18	594.508	594
19	563.218	563
20	535.058	535
21	509.578	510
22	486.416	487

Table 3. Calculated and actual wavelengths of HH band luminescence.

m	$\lambda_{\text{cal}}(\text{nm})$	$\lambda_{\text{exp}}(\text{nm})$
17	621.114	621
18	586.608	586
19	555.733	555
20	527.994	528
21	502.806	503
22	479.952	480

Figure 7 demonstrates the correspondence between the simulated reflectance spectra of the cavity and the experimental EL spectra, with mode group I representing the LH band luminescence and mode group II representing the HH band luminescence. It can be seen that the simulated results coincide well with the experimental results, which demonstrates the high quality of the resonance cavity of our MCLEDs.

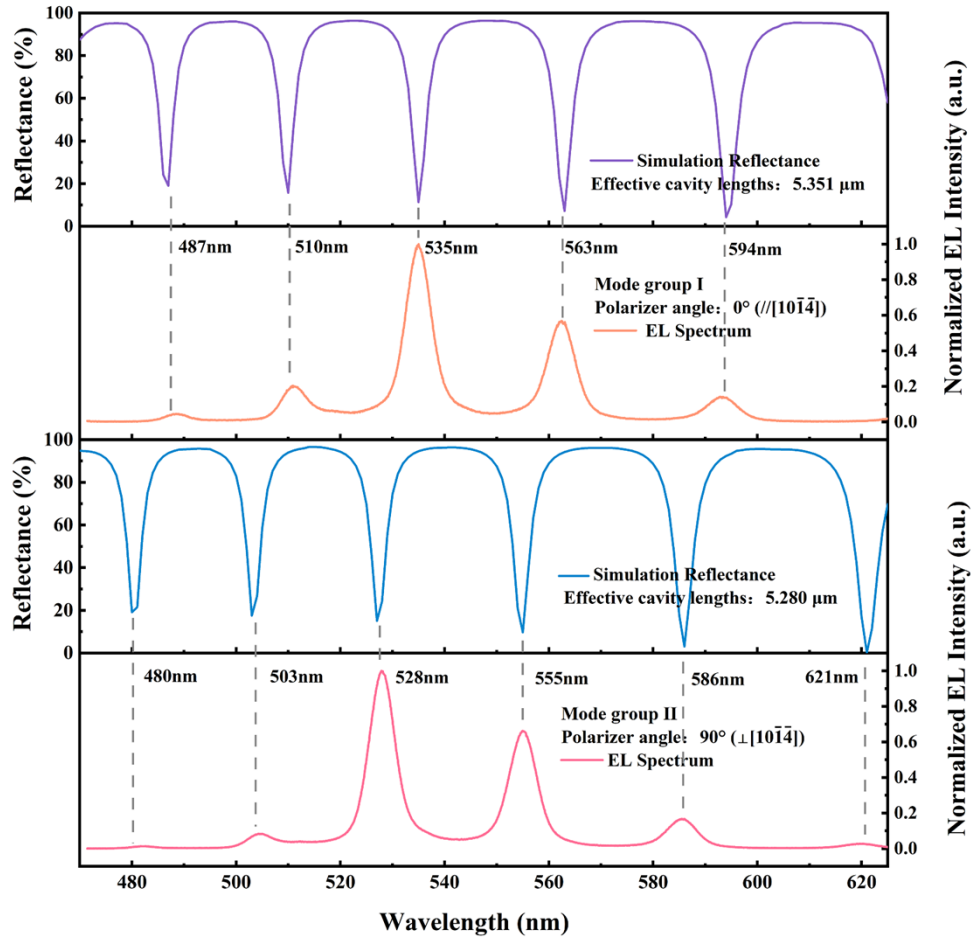


Fig. 7. The simulated reflection spectra and normalized EL intensity plots of Mode Group I and II

A comparative analysis of the divergence angle between the MCLED in this study and a conventional MLED without cavity was also conducted. Figures 8(a) and (b) illustrate the contour maps of the EL far-field distribution for MCLED and conventional MLED. It is observed that the cavity mode wavelength of MCLED shifts with the emission angle and the intensity distribution of the emitted light is relatively concentrated. In contrast, the intensity distribution of conventional MLED is more dispersed. Figure 8(c) presents a comparative result of the emission intensity as a function of detection angle of the MCLED and conventional MLED. The divergence angle of MCLED is approximately 80° , which is significantly reduced compared to the that of conventional MLEDs ($\sim 130^\circ$). The reduced divergence angle of MCLED is primarily attributed to the resonant cavity structure, which enhances the vertical emission of light.

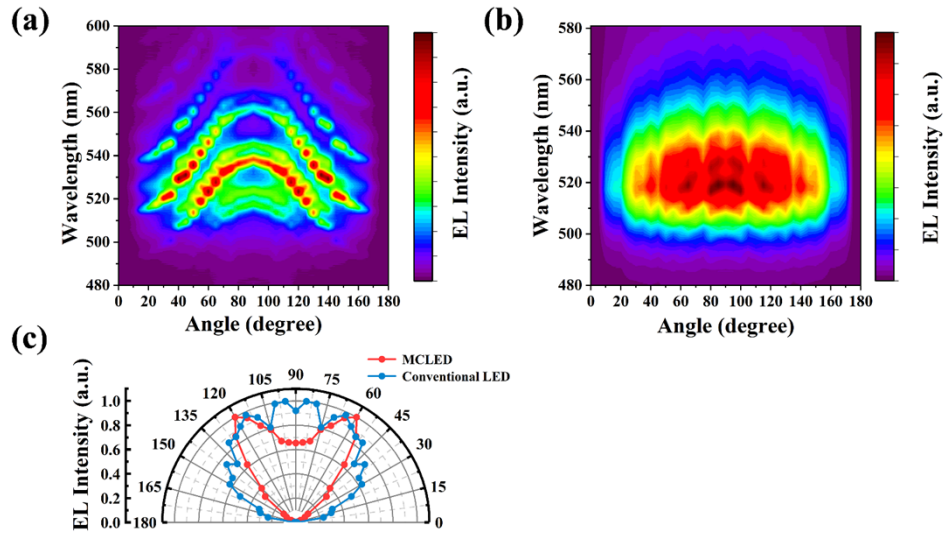


Fig. 8. (a) Contour map of the EL intensity far-field distribution for MCLED. (b) Contour map of the EL intensity far-field distribution for the conventional LED. (c) Graphical comparison of the divergence angles between MCLED and conventional LED.

2.3. Orthogonal polarization emission characteristics of MCLED parallel arrays

To improve the output power of such orthogonally polarized light sources, 2×2 and 3×3 parallel MCLED arrays were also fabricated. Figure 9(a) illustrates the EL spectra of the 3×3 MCLED array under different current. Similar with the single device, the spectrum clearly exhibits the mode splitting phenomenon. Figure 9(b) presents the I-V curve and luminescence image of the 3×3 array. As observed in the figure, the emission intensity from different devices of the array is relatively uniform. Figures 9(c) and (d) illustrate the polarization characteristics of the MCLED array. The device array maintains well the orthogonal polarization properties, with mode groups I and II exhibiting high polarization ratio of 0.67 and 0.82, respectively. The polarization ratio of the array is somewhat smaller compared to a single device. This can be explained by the interference of a background emission. The cavity modes of the array are superimposed on top of a broad background luminescence, as shown in Fig. 10(a). On the other hand, the background emission of a single device is less obvious, as shown in Fig. 10(b). The broad background emission can be originated from the spontaneous emission escaped from the sidewall of the device, which are featured with low polarization ratio. The emission spectra of device array are a combination of cavity modes and a broad spontaneous background emission. Therefore, the polarization ratio of the array (0.67 and 0.82) is lower than that of a single device (0.85 and 0.89).

due to the “spectral interference”. To suppress the light leakage and background emission, high reflectivity coatings (e.g., metallic coatings) can be deposited on the sidewall of the device in the future work.

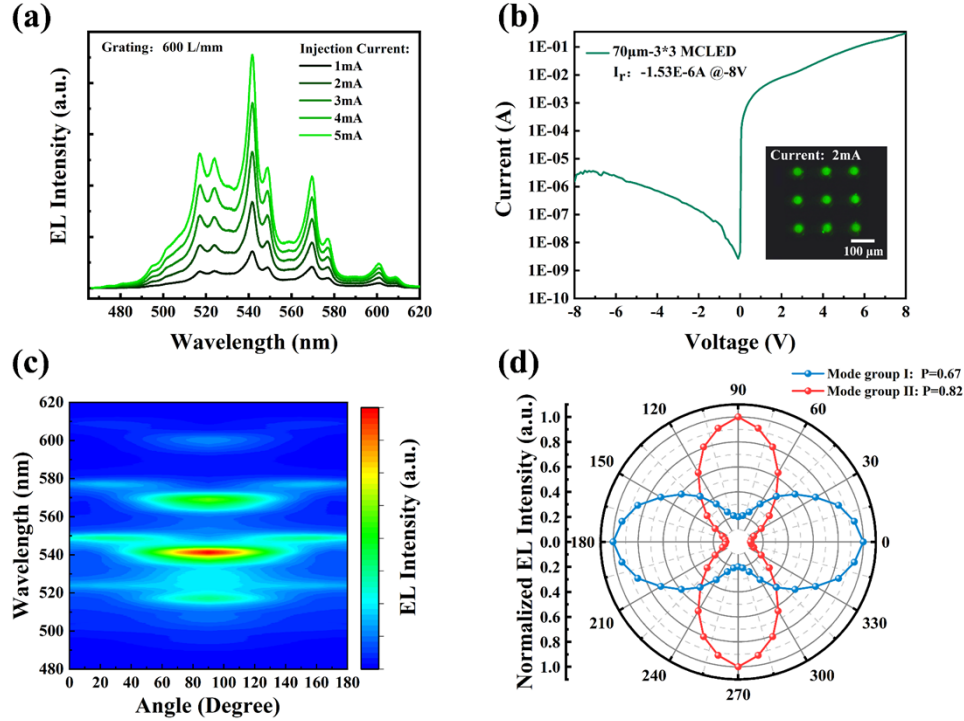


Fig. 9. (a) EL intensity of the MCLED array. (b) I-V characteristic curve and luminescence image of the array. (c) EL intensity map of the MCLED array. (d) Polar plot of the normalized EL intensity in polar coordinates.

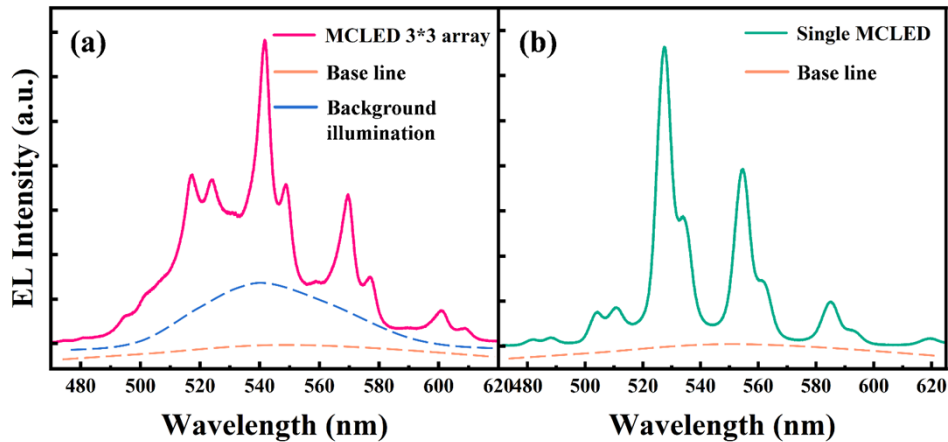


Fig. 10. EL spectra of a single MCLED with a 3*3 array at 5 mA current MCLED arrays with grid electrode structure

Figure 11 presents the light output power of different MCLED arrays and single-device under different current density. Due to the single QW structure of the epitaxial wafer, the light output power of an individual MCLED is merely 0.07 mW under 1400 A/cm². When the devices are connected in parallel to form arrays, a 2*2 array demonstrates a light output power of 0.29 mW, while the power output of a 3*3 array is further augmented to 0.66 mW, which is significantly higher compared to single devices. This work validates the substantial advantage of the array structure in terms of light output power while maintaining the orthogonal polarization performance, which is essential for MCLED devices in high-power applications.

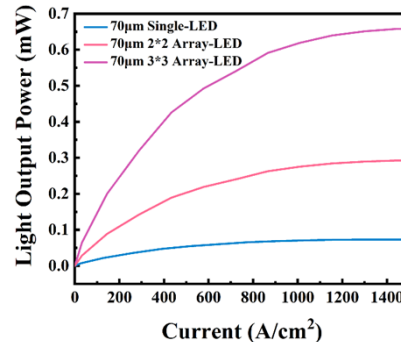


Fig. 11. Comparative analysis of the light output power between MCLED arrays and a single LED device.

3. Conclusion

In summary, MCLEDs and their arrays based on semi-polar InGaN/GaN structure are fabricated, which are capable of emitting orthogonally polarized light. The devices are featured with SiO₂/TiO₂ top DBR and Ag bottom mirror, which not only effectively enhance the thermal dissipation performance of the device but also ensure the achievement of high polarization ratio. Furthermore, the MCLED array significantly increases the light output power while maintaining the orthogonal polarization characteristic, providing a novel approach for high-power light source applications in fields such as visible light communication and 3D display. These findings offer critical insights into the novel performance of MCLED devices and their potential for practical applications.

Funding. National Natural Science Foundation of China (62474150, U21A20493, 62234011); National Key Research and Development Program of China (2024YFB3613100); Natural Science Foundation of Fujian Province (2023J05020); Natural Science Foundation of Guangdong Province (2025A1515011349).

Disclosures. The authors declare no conflicts of interest

Data availability. Data underlying the results presented in this paper are not publicly available at this time but may be obtained from the authors upon reasonable request.

References

1. D. A. Japuntich, "Polarized task lighting to reduce reflective glare in open-plan office cubicles," *Applied Ergonomics* **32**(5), 485–499 (2001).
2. Y. D. Lin, Q. Y. Du, L. Q. Tong, *et al.*, "Usability of Using Polarized Filter for Reading Lamp to Reduce Disturbing Reflected Glare," *Appl. Mech. Mater.* **58-60**, 787–792 (2011).
3. D. Mace, P. Garvey, R. J. Porter, *et al.*, "Countermeasures for reducing the effects of headlight glare," *J American Automobile Association Foundation for Traffic Safety* **1** (2001).
4. M. Heger, J. F. Beek, K. Stenback, *et al.*, "Darkfield orthogonal polarized spectral imaging for studying endovascular laser-tissue interactions in vivo-a preliminary study," *Opt. Express* **13**(3), 702–715 (2005).
5. B. Ozdilek, B. Zoroglu, A. S. Turk, *et al.*, "Infrared Polarized Light Application in the Chronic Migraine Treatment: Safety and Effectiveness," *Acupunct. Electro-Ther. Res.* **48**(3), 213–223 (2023).

6. H. J. Cornelissen, H. J. B. Jagt, D. Broer, *et al.*, "Efficient and cost-effective polarized-light backlights for LCDs," in *Eighth International Conference on Solid State Lighting*, (SPIE, 2008), 187–196.
7. X. Li, Z. Liu, Y. Cai, *et al.*, "Polarization 3D imaging technology: a review," *Front. Phys.* **11**, 1198457 (2023).
8. H. Kaur and N. S. Grewal, "Ultra high-speed VLC system using polarization division multiplexed QPSK, DSP, and matched filters," *Opt. Quant. Electron.* **54**(10), 636 (2022).
9. Z. Zhou, B. Bai, and L. Liu, "Silicon on-chip PDM and WDM technologies via plasmonics and subwavelength grating," *IEEE J. Sel. Top. Quantum Electron.* **25**(3), 1–13 (2019).
10. G. A. Atkinson and E. R. Hancock, "Shape estimation using polarization and shading from two views," *IEEE Trans. Pattern Anal. Machine Intell.* **29**(11), 2001–2017 (2007).
11. Y. Huo, J. Guan, R. Dang, *et al.*, "Polarization-enhanced contrast imaging for pupil detection," *Optics Lasers in Engineering* **184**, 108595 (2025).
12. Y. Tomita and S.-s. Matsushima, "Photorefractive beam coupling between orthogonally polarized light beams by linear dichroism in Cu-doped potassium sodium strontium barium niobate," *J. Opt. Soc. Am. B* **16**(1), 111–116 (1999).
13. L. Nedelchev, E. Stoykova, G. Mateev, *et al.*, "Photoinduced chiral structures in case of polarization holography with orthogonally linearly polarized beams," *Opt. Commun.* **461**, 125269 (2020).
14. Y. Zhang, Z. Hao, L. Wei, *et al.*, "Image edge-enhancement using orthogonally polarized light," in *International Symposium on Photoelectronic Detection and Imaging 2007: Image Processing*, (SPIE, 2008), 187–192.
15. W. Groner, J. W. Winkelman, A. G. Harris, *et al.*, "Orthogonal polarization spectral imaging: a new method for study of the microcirculation," *Nat. Med.* **5**(10), 1209–1212 (1999).
16. J.-T. Oh and S.-W. Kim, "Polarization-sensitive optical coherence tomography for photoelasticity testing of glass/epoxy composites," *Opt. Express* **11**(14), 1669–1676 (2003).
17. C. Sturesson, J. Nilsson, and S. Eriksson, "Non-invasive imaging of microcirculation: a technology review," *Med. Devices: Evidence Res.* **7**, 445–452 (2014).
18. K. Khare, M. Butola, S. Rajora, *et al.*, *Fourier optics and computational imaging* (Springer, 2015).
19. D. Iida, S. Lu, S. Hirahara, *et al.*, "Enhanced light output power of InGa_N-based amber LEDs by strain-compensating AlN/AlGa_N barriers," *J. Cryst. Growth* **448**, 105–108 (2016).
20. D. Iida, K. Niwa, S. Kamiyama, *et al.*, "Demonstration of InGa_N-based orange LEDs with hybrid multiple-quantum-wells structure," *Appl. Phys. Express* **9**(11), 111003 (2016).
21. B. Monemar, "Fundamental energy gap of GaN from photoluminescence excitation spectra," *Phys. Rev. B* **10**(2), 676–681 (1974).
22. C. Zhang, K. Xiong, G. Yuan, *et al.*, "A resonant-cavity blue-violet light-emitting diode with conductive nanoporous distributed Bragg reflector," *Phys. Status Solidi* **214**(8), 1600866 (2017).
23. H. Masui, S. Nakamura, S. P. DenBaars, *et al.*, "Nonpolar and semipolar III-nitride light-emitting diodes: Achievements and challenges," *IEEE Trans. Electron Devices* **57**(1), 88–100 (2010).
24. S. E. Brinkley, Y.-D. Lin, A. Chakraborty, *et al.*, "Polarized spontaneous emission from blue-green m-plane GaN-based light emitting diodes," *Appl. Phys. Lett.* **98**(1), 3541655 (2011).
25. H. Masui, H. Yamada, K. Iso, *et al.*, "Optical polarization characteristics of InGa_N/ GaN light-emitting diodes fabricated on GaN substrates oriented between (10 $\bar{1}$) and (101 $\bar{1}$) planes," *Appl. Phys. Lett.* **92**(9), 2890050 (2008).
26. H. Yan, Z. Gan, and S. Liu, "Influence of strains on the optical properties of non-polar and semi-polar gallium nitride based LEDs," in *2012 13th International Conference on Electronic Packaging Technology & High Density Packaging*, (IEEE, 2012), 1620–1623.
27. T. Kyono, Y. Yoshizumi, Y. Enya, *et al.*, "Optical polarization characteristics of InGa_N quantum wells for green laser diodes on semi-polar {20 $\bar{1}$ } GaN substrates," *Appl. Phys. Express* **3**(1), 011003 (2010).
28. H. Li, P. Li, H. Zhang, *et al.*, "Electrically driven, polarized, phosphor-free white semipolar (20-21) InGa_N light-emitting diodes grown on semipolar bulk GaN substrate," *Opt. Express* **28**(9), 13569–13575 (2020).
29. C.-W. Hsu, C.-H. Yeh, C.-W. Chow, *et al.*, "Using adaptive equalization and polarization-multiplexing technology for gigabit-per-second phosphor-LED wireless visible light communication," *Opt. Laser Technol.* **104**, 206–209 (2018).
30. W. Ou, Y. Mei, H. Long, *et al.*, "Orthogonally and linearly polarized green emission from a semipolar InGa_N based microcavity," *Nanophotonics* **13**(1), 75–83 (2024).
31. E. A. Amargianitakis, K. Tsagaraki, A. Kostopoulos, *et al.*, "Non-polar GaN/AlGa_N quantum-well polariton laser at room temperature," *Phys. Rev. B* **104**(12), 125311 (2021).
32. Y. Mei, Z. Zheng, S. Yang, *et al.*, "Fabrication of GaN-based micro-cavity light emitters," in *2023 Opto-Electronics and Communications Conference (OECC)*, (IEEE, 2023), 1–4.
33. W. Ou, Y. Mei, D. Iida, *et al.*, "InGa_N-based orange-red resonant cavity light-emitting diodes," *J. Lightwave Technol.* **40**(13), 4337–4343 (2022).
34. S. Yang, H. Xu, H. Long, *et al.*, "GaN-based green resonant-cavity light-emitting diodes with Al mirror and copper plate," *Opt. Lett.* **47**(11), 2858–2861 (2022).
35. S. Zhu, X. Shan, R. Lin, *et al.*, "Characteristics of GaN-on-Si green micro-LED for wide color gamut display and high-speed visible light communication," *ACS Photonics* **10**(1), 92–100 (2023).
36. S.-W. H. Chen, Y.-M. Huang, Y.-H. Chang, *et al.*, "High-bandwidth green semipolar (20–21) InGa_N/GaN micro light-emitting diodes for visible light communication," *ACS Photonics* **7**(8), 2228–2235 (2020).

37. W. Tian, Y. Wu, T. Wu, *et al.*, “Optical–electrical characteristic of green based on GaN micro-LED arrays,” *Appl. Opt.* **61**(19), 5666–5674 (2022).
38. M. Kubota, K. Okamoto, T. Tanaka, *et al.*, “Temperature dependence of polarized photoluminescence from nonpolar m-plane InGaN multiple quantum wells for blue laser diodes,” *Appl. Phys. Lett.* **92**(1), 011920 (2008).
39. E. Matioli, S. Brinkley, K. M. Kelchner, *et al.*, “High-brightness polarized light-emitting diodes,” *Light: Sci. Appl.* **1**(8), e22 (2012).
40. L. Jiang, J. Liu, L. Zhang, *et al.*, “Suppression of substrate mode in GaN-based green laser diodes,” *Opt. Express* **28**(10), 15497–15504 (2020).